0.2-10 keV X-ray measurements on the PFRC-2: EEDF, heating, and confinement

B. Alessio[1], C. Swanson[2], K. Torrens[1], E.S. Evans [3], and S.A. Cohen[3]

[1]**Princeton University**
[2]**Princeton Satellite Systems**
[3]**Princeton Plasma Physics Laboratory**

ABSTRACT

Time and spatially resolved X-Ray spectra from odd-parity RMF-heated hydrogen plasma in the PFRC-2 were obtained with in-house-calibrated silicon-drift detectors (SDD). Both Bremsstrahlung and line radiation were observed. Maxwellian-fit electron density and temperature were extracted from the Bremsstrahlung segment of the spectra using a Poisson-regularized inversion method. Temperatures of a minority component exceeded 600 eV. The rate-of-rise of the electron energy was used as a proxy for the effectiveness of the heating process and quality of confinement. Line emission showed the presence of carbon, oxygen, iron, and nitrogen. The brightness values of these line emissions were sensitively dependent upon applied magnetic field strength, gas fill pressure, pumping method, and boundary conditions. Conditions were found where the SDD viewing through the axial midplane of the plasma measured an X-ray brightness as much as 100x greater than that measured by an SDD viewing 5 cm away from the midplane. Possible causes, including non-uniform electron energization, plasma shape changes, and plasma-wall interactions, for this disparity are discussed.

Keywords: Field-Reversed Configuration, Electron Energy Distribution Function, X-ray Count Rate, Silicon Drift Detector

1 THE PRINCETON FIELD-REVERSED CONFIGURATION

The mission of the Princeton Field Revered Configuration (PFRC) is to create clean and small fusion reactors. It employs the Field-Reversed configuration to confine plasma, which is simple in comparison to tokamaks and promises to be mobile and is well-suited for aneutronic reactions such as the Deuterium and Helium-3 because it confines high-β plasma (Cohen et al., 2007). The Field-Reversed configuration, depicted in Figure 1, forms at the minimum in a magnetic mirror upon odd parity rotating magnetic field (RMF) pulsing at radiofrequency and pushes the plasma to high temperature and density, where the end goal is to reach the critical values of temperature and density to induce fusion.

The research discussed in this paper took place on the second prototype of the PFRC, which is referred to as the PFRC-2. Figure 2 displays the experimental layout of the PFRC-2. The gas to be ionized is fed into the center cell from the source region. The magnetic mirror forms fron the L-2 coils at $z = \pm 50$ and is pinched off by nozzle coils. The Source End Cell (SEC) and the Far End Cell (FEC) form from the end coils at $z = \pm 100$. The X-ray detectors have lines of sight through the midplane and 5cm displaced in the negative z direction. Langmuir probes in the SEC and the FEC measure the outgoing electron density while the cup in the SEC and the paddle in the FEC measure the outgoing voltage.

2 PLASMA X-RAY EMISSIONS

Plasma generates X-rays in two ways. One is through k-alpha and l-alpha spectral line emissions from the various elements in the plasma. The other is through Bremsstrahlung emissions that come about when electrons decelerate around ions in the plasma. Recording the 0.2-10 keV X-ray emissions of the plasma in the PFRC is important because they give information on the temperature and density of the plasma.

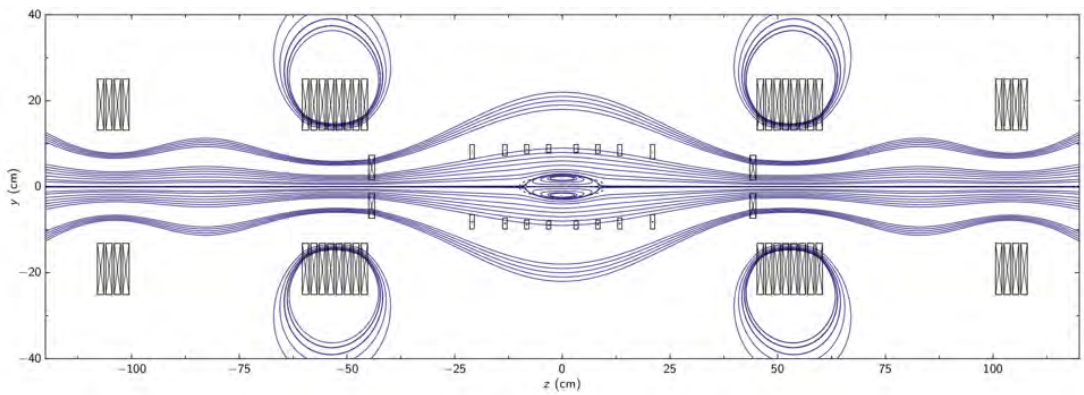

Figure 1. A bird's eye view of the magnetic field lines of the PFRC-2. The sources of magnetic field are the L-2 coils, the nozzle coils, and the plasma. The FRC is seen at the center, of separatrix radius r_s. The magnetic field at $z = y = 0$ is discontinuous as the field reverses direction.

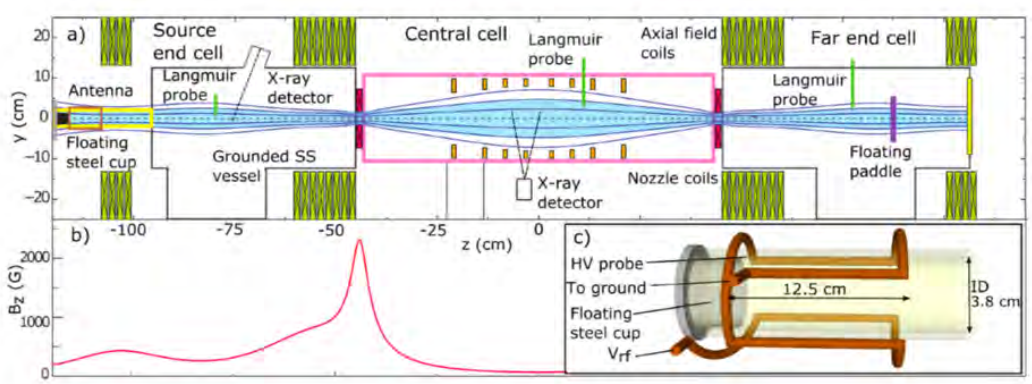

Figure 2. (a) The experimental setup of the PFRC-2. (b) Typical axial profile of the magnetic field. (c) Source region with double-saddle antenna (Jandovitz et al., 2018)

2.1 Silicon Drift Detectors

The apparatus used to record the X-ray emissions was the Silicon Drift Detector (SDD). Two in-house-calibrated SDDs were placed on the PFRC-2. One was placed to view the midpoint of the FRC from an 8.5-degree angle. The other was displaced 5cm in the negative z-direction. The midpoint detector had on its interface with the vacuum vessel a thin movable metal plate with 5 apertures of varying size, each five times smaller in area than the next. The 5cm displaced detector had a rotating mount that allowed a radial scan.

2.2 X-ray spectra

Figure 3 is an example X-Ray spectrum between 0.2 and 30 keV, measured by the midpoint detector, normalized by time and sorted into energy bins. At energies lower than 1 keV, the spectral emissions dominate spectrum, obscuring the Bremsstrahlung emissions. Carbon, Nitrogen, Oxygen, and Iron are all apparent, with Gaussian distributions centered at their emission energy shown by the red lines in Figure 3. The reason for the Gaussian distribution is the counting statistics of the SDD as it counts electrons freed by the incoming X-rays. At energies above 1 keV, the Maxwellian form of the Bremsstrahlung is seen. The detector was set to ignore any signal below 0.2 eV to prevent electrical noise from obscuring the spectrum.

2.3 Electron Energy Distribution Function from X-ray spectrum inversion

This section will discuss obtaining the Electron Energy Distribution Function (EEDF) from the measured X-ray Energy Distribution Function (XEDF). For a more in-depth explanation, see Dr. Charles Swanson's paper on the inversion method (Swanson et al., 2018).

The XEDF $l(\vec{a})$ is linear in EEDF $\vec{a}$. As the XEDF is measured discretely, it is transformed into the EEDF by matrix $\mathbf{M}$. In order to obtain the most likely EEDF given a truncated Maxwellian of discrete values, one must minimize the following cost function with respect to $\vec{a}$:

$$C(\vec{a}) = \sum_i [(\mathbf{M}\vec{a})_i - \mathbf{b_i} ln(\mathbf{M}\vec{a})_i] \tag{1}$$

where $\vec{a}$ is the vector of EEDF values, $\mathbf{b}$ is the matrix of measured XEDF values, and $\mathbf{M}$ transforms the XEDF into the EEDF.

Figure 4 is an example of an XEDF and its EEDF as generated by Dr. Swanson's method implemented in MATLAB. The blue line is the XEDF and the yellow line is the EEDF. The top right corner includes the electron temperature and density associated with the generated EEDF.

2.4 Expected X-ray Count Rate

These detectors gave X-ray energy distribution and X-ray count rate measurements. The expected X-ray count rate is:

$$CR_{\text{expected}} = \rho L_1 A_1 \frac{A_2}{4\pi L_2^2} \tag{2}$$

Where ρ is the plasma X-ray count rate per volume, L_1 is the length of plasma in the line of sight of the SDD, A_1 is the area of the aperture, A_2 is the area of the detector, and L_2 is the length of the telescope between the aperture and the detector.

CR_{expected} is to be observed in the system depicted in Figure 5. Inherent in this model's treatment of plasma length is the use of the line average along the line of sight of the detector. The spectra observed by the SDDs do not indicate the variation in electron temperature and density along the line of sight of the detector.

2.5 More Derived Parameters

In addition to X-ray count rate, derived parameters included X-ray count rate above an energy threshold (typically around 1 keV), average X-ray energy above an energy threshold (typically 1 keV), and the Maxwellian-fit electron density and electron temperature.

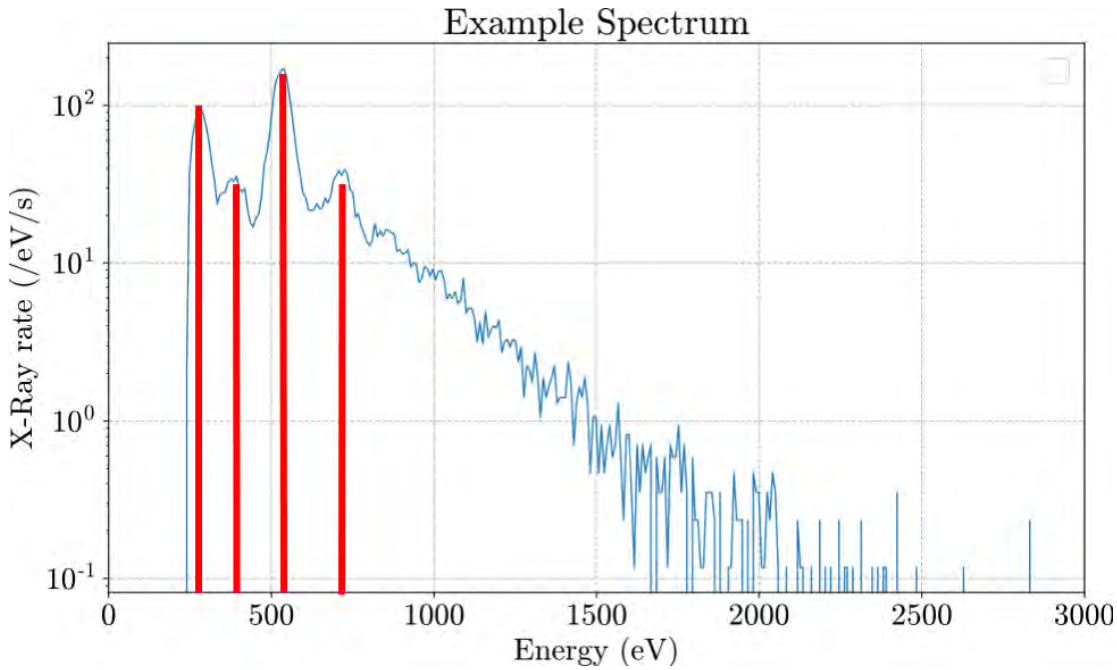

Figure 3. An example X-ray spectrum with spectral line emissions observed by the midplane SDD. The line emissions are from, in order of increasing energy, Carbon, Nitrogen, Oxygen, and Iron.

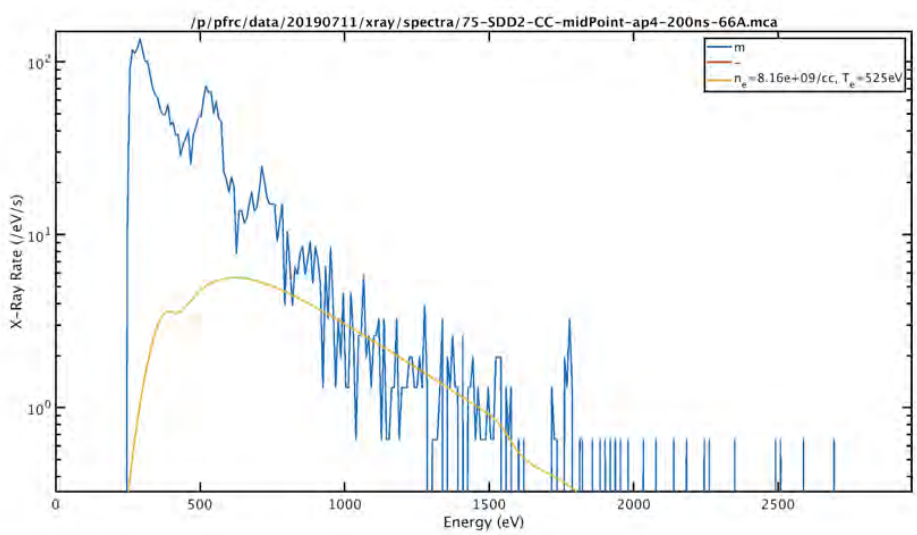

Figure 4. An example X-ray spectrum with the EEDF generated from the truncated distribution of Bremsstrahlung emissions.

The X-ray count rate above the energy threshold is expressed as the following:

$$CR_{\text{threshold}}(\vec{C},\vec{E}) = \frac{1}{t_{\text{accum}}}\sum_{i=0}^{n} C_i\Theta(E_{\text{i}} - E_0) \tag{3}$$

where t_{accum} is the accumulation time of the spectrum, $\vec{C}$ is the n-dimensional vector of X-ray counts in energy bin i, $\vec{E}$ is the n-dimensional vector of the energy of bin i, E_0 is the threshold energy, and Θ is the Heaviside step function.
The average X-ray energy above the energy threshold is expressed as the following:

$$E_{\text{threshold}}(\vec{C},\vec{E}) = \frac{1}{n}\sum_{i=0}^{n} C_{\text{i}}E_{\text{i}}\Theta(E_{\text{i}} - E_0) \tag{4}$$

where $\vec{C}$ is the n-dimensional vector of X-ray counts in energy bin i, $\vec{E}$ is the n-dimensional vector of the energy of bin i, E_0 is the threshold energy, and Θ is the Heaviside step function.
The average X-ray energy above the threshold was found to follow the same trends of the Maxwellian-fit electron temperature, despite the two being independent derived parameters. This is shown in Figures 6 and 7, which show an inconclusive but characteristic relationship between the seed plasma power and the X-ray energies for high and low center cell pressure. The characteristic trend, which can be attributed to high levels of uncertainty in the measurement, is consistent between the average X-ray energy above a threshold and the Maxwellian-fit electron temperature. A program was written in Python to derive these parameters from the SDD measurements and the plot and analyze them.

3 OBSERVATIONS

3.1 Grounded Diamagnetic Loop

The changes in spectra for varying parameters and setups on the PFRC-2 were often observed in only certain energy regions. When grounding a diamagnetic loop and comparing the observed X-ray spectrum to that with the floating loop, significant change occured only in the spectral line emission region (below 1 keV). As seen in Figure 8, the line emissions increased by an order of magnitude and the signal was dominated by Oxygen emissions when the diamagnetic loop was grounded, but the Bremsstrahlung emissions appeared unchanged. This was possibly the result of the grounded diamagnetic loop providing a pathway for plasma collision into a more Oxygen-rich region of residual gas or wall.

3.2 Record Maxwellian-fit Electron Temperature

Prior to installing belt coils on the PFRC-2 (see later section), the highest Maxwellian-fit electron temperature derived from observed spectra was 670 eV for RMF power 71 kW, L-2 coil current 104 A, and center cell pressure 0.432 mTorr. As seen in Figure 9, there was a peak in X-ray count rate between 1.58 ms and 2.3 ms after the start of the RMF pulse corresponding to this calculation. Averaging over time gave an unremarkable Maxwellian-fit electron temperature. Figure 10 shows the time behavior of the electron density measured in the center cell throughout the RMF pulse. The region corresponding to the X-ray count rate peak is enclosed by the red circle. The flatness of the density indicates that either very little plasma leaked throughout this time window or there was increased ionization from more gas. Additionally, Figure 11 shows the X-ray spectrum of just this time window, which has no apparent line emissions in the lower energy region. A possible conclusion is that there was little to no Carbon, Oxygen, Iron, and Nitrogen impurities present in the plasma during this time window. Further, this implies that the impurities have the undesirable effect of cooling down the plasma.

3.3 Center Cell Pressure

The gas in the center cell is the fuel for making plasma to form the FRC, but too high of a pressure can suppress the phase transition from occurring without more RMF power. This balance causes there to be local minima and maxima but a general increase in X-ray production as pressure increases. This is seen in Figure 12 with the maximium at 0.35 mTorr and the minimum at 1.00 mTorr, for an L-2 coil current of 102 A and an RMF power of 45 kW. Figure 13 shows how the average X-ray energy above

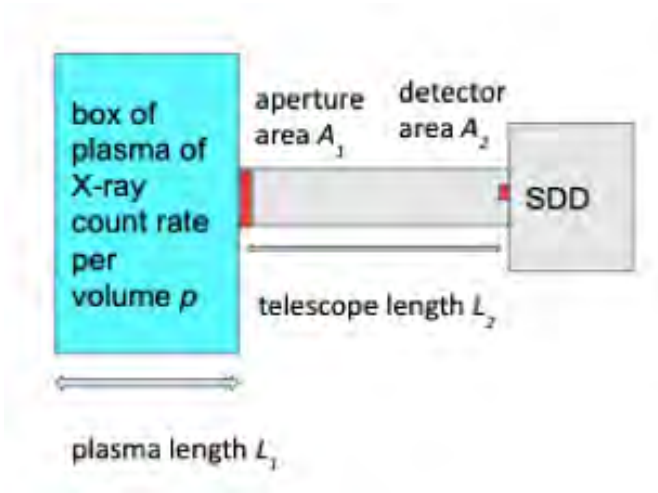

Figure 5. A model of X-ray emission from the plasma and detection by an SDD.

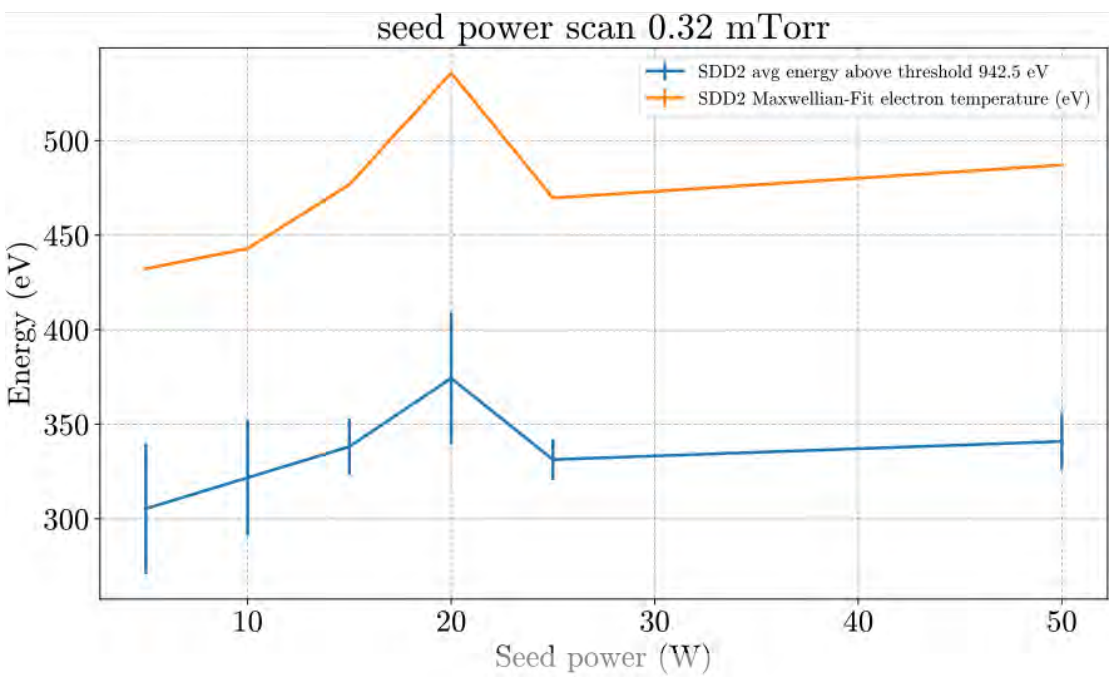

Figure 6. Seed plasma power scan at 0.32 mTorr center cell pressure for average X-ray energy above a 942.5 eV (eq. 4) and Maxwellian-fit electron temperature, two independent derived parameters.

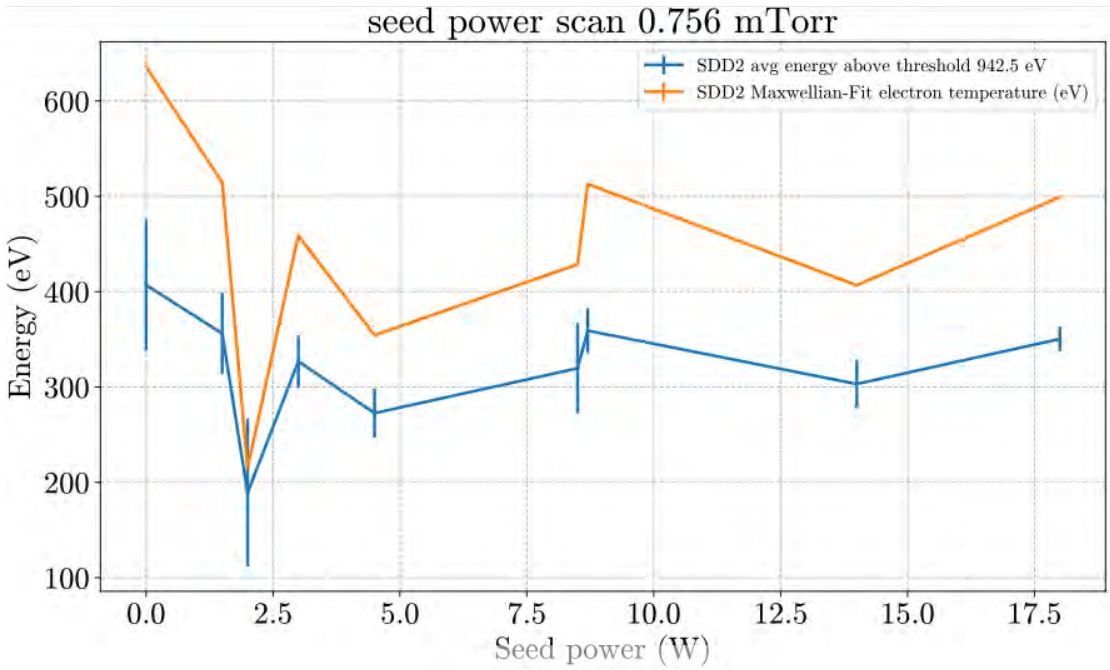

Figure 7. Seed plasma power scan at 0.756 mTorr center cell pressure for average X-ray energy above a 942.5 eV (eq. 4) and Maxwellian-fit electron temperature, two independent derived parameters.

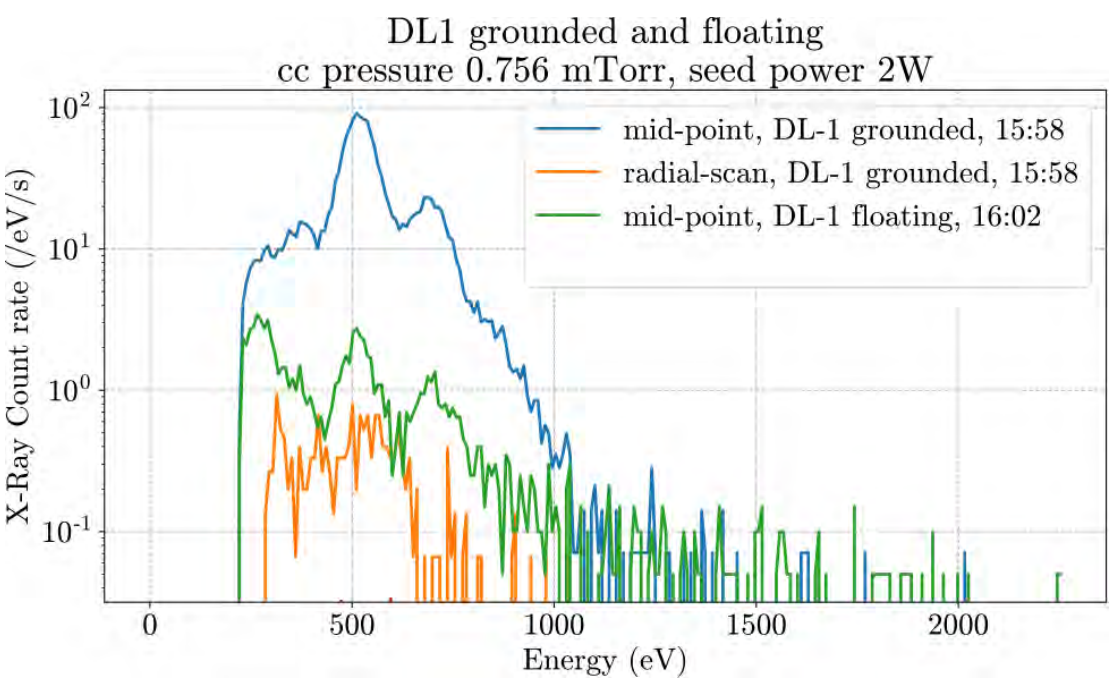

Figure 8. X-ray spectra in both SDDs for floating and grounding diamagnetic loop.

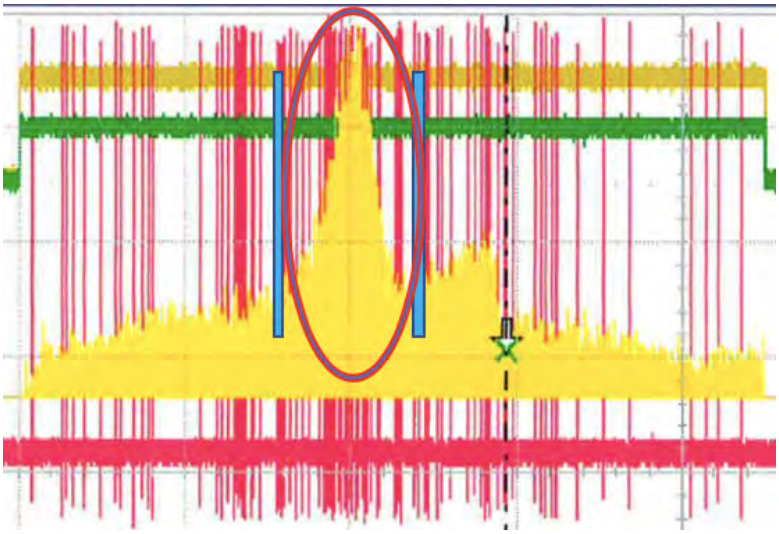

Figure 9. Time evolution of X-ray count rate throughout the RMF pulse, accumulated over many pulses. Region of interest is identified by the blue bars and red oval.

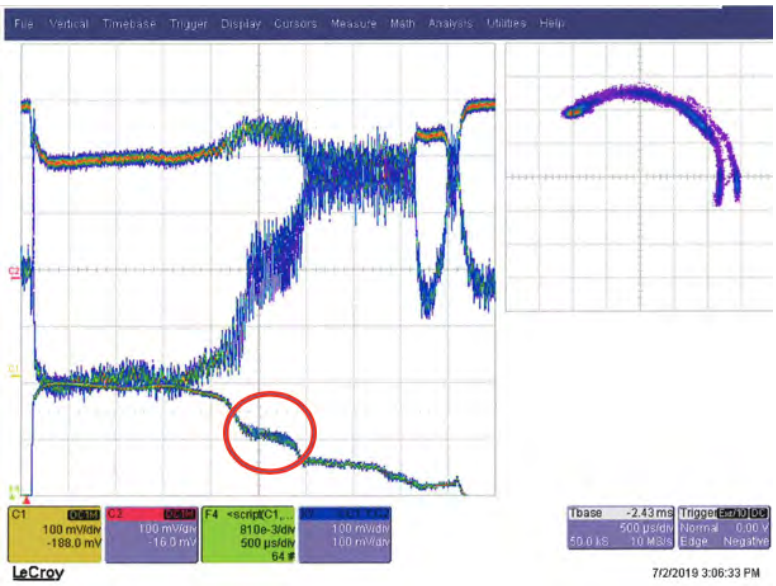

Figure 10. The time evolution of the electron density measured in the center cell throughout the RMF pulse. Region of interest identified by red circle.

the threshold follows the opposite trend as the X-ray count rate for up to 0.50 mTorr, and the same trend (within the error bars) for above 0.50 mTorr. A possibility is that the lower center cell pressure is harder to keep constant, leaving the high energy values and X-ray production sensitively dependent on other conditions, such as the time evolution of the pressure. This could be attributed to plasma contact with the wall. However, at higher pressures, both of these parameters tend to increase with pressure.

3.4 Midplane Silicon Drift Detector Aperture Discrepancy

The midplane SDD had five aperture settings at its interface with the center cell. Each aperture was 5x smaller in area than the next, and the last setting (the open setting) had no aperture. For an L-2 coil current of 97 A, an RMF power of 45 kW, and a center cell pressure of 0.34 mTorr, there was a discrepancy between the open setting and all of the others. As Figure 14 shows, the X-ray spectrum associated with the open setting matches the spectra associated with settings three and four for energies above 500 eV, but is nearly an order of magnitude higher for energies below 500 eV. Figure 15 shows a close up of the region of discrepancy and includes the averaged time evolution throughout the RMF pulse of the X-rays for each spectrum. The open setting's time evolution has a clear dip in the first half and a large and sudden increase in the second half. Settings three and four appear more flat but also have far fewer X-rays recorded. This is because the smaller apertures restrict the count rate as described above. For this reason, the first and second aperture setting observations were not included, as there were not enough X-rays recorded. A possibility is that the open setting sees more Carbon spectral lines than the others. This is supported by the fact that the only distinguished spectral line emission in the region of the discrepancy is Carbon. Another possible explanation is an oblate FRC, as depicted in Figure 16. The line of sight, through which the observations are averaged, of the midplane detector may include significantly more cold plasma when the aperture is set to open, which would include more Carbon and other impurities. This would mean the oblate FRC was approximately a wall for the lines of sight of the first through fourth aperture settings, but has significant curvature in the line of sight of the open aperture setting, and the curvature changes the ratio of oblate FRC to cold plasma observed by the detector. This would imply that the FRC was unstable and also had a minor radius within an order of magnitude of the open aperture's radius. Some other possibilities include a very small prolate FRC with central motion giving an oblate appearance, a prolate bulk FRC with a hot o-point, or a large FRC that collides with walls on the midplane.

4 FRC FORMATION AT HIGH MAGNETIC FIELD

Due to their greater mass and the $m^{\frac{1}{2}}$ dependence of the gyro-radius, ions require a higher magnetic field than electrons to be confined. For this reason, the PFRC-2 was exclusively heating electrons by setting the RMF frequency well above the ion cyclotron frequency, while research was being done to determine how best to get to higher temperature and density at higher confining magnetic field. This presented a challenge at low RMF power, as the measured X-ray count rate at higher confining magnetic field decreased in comparison to lower confining magnetic field. Figure 17 shows the relationship between X-ray count rate and confining magnetic field from the L-2 coils at varying center cell pressure for 30 kW of RMF power. The higher confining magnetic field severely restricted plasma formation, as very few X-rays are seen above 100A in the L-2 coils, regardless of center cell pressure. Furthermore, the measurements above 300A in the L-2 coils for 60 kW of RMF power, as in Figure 18, show an anomalous trend that differs from the tendency of higher magnetic field to cause a lower count rate. This could possibly be the lack of a formation of an FRC, with more emissions from the seed plasma instead.
Additionally, the discrepancy between the X-ray count rates observed by both the midplane SDD and the 5cm displaced SDD, as seen in Figure 19, brought into question the size of the FRC. Only at the higher confining field, where the anomalous trend emerges, does the displaced detector begin to see a non-negligible number of X-rays. This suggests that the FRC itself was smaller than 5cm in radius and left its geometry to be determined.

4.1 Belt Coil Design

The challenge of describing the shape and size of the FRC was complicated by the limited setup of two SDDs. However, a new approach was conceived, designed, and implemented: adding belt coils closer to the center of the FRC than the L-2 coils in such a way as to break the symmetry of the PFRC-2 so that the FRC would form away from the midplane SDD and closer to the 5cm displaced detector, as depicted in Figure 20. By moving the magnetic minimum of the PFRC-2 along the z-axis and performing a radial

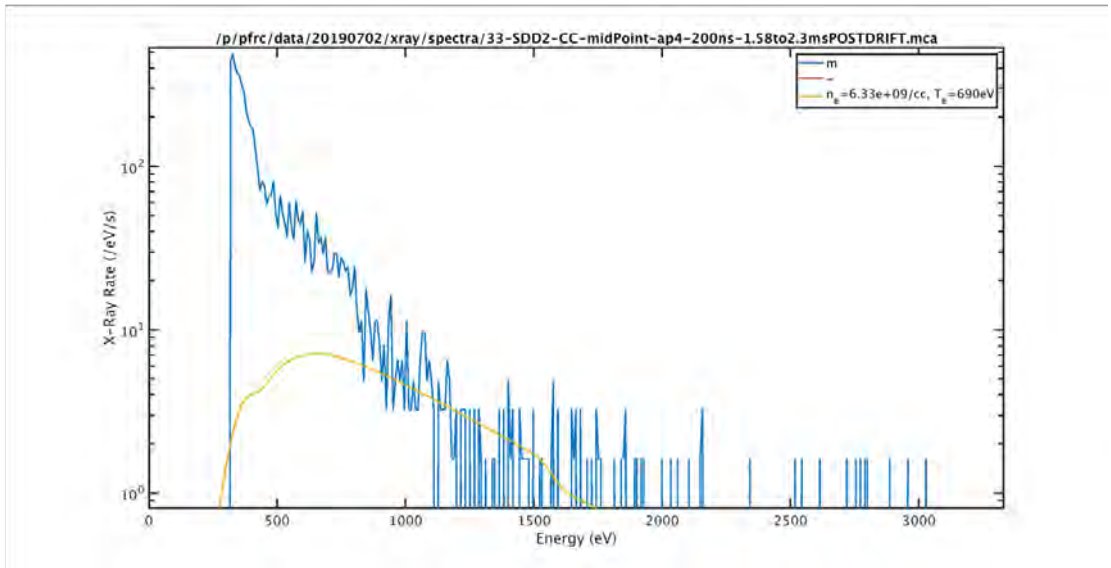

Figure 11. X-ray spectra for the 1.58 ms to 2.3 ms time window in the RMF pulse.

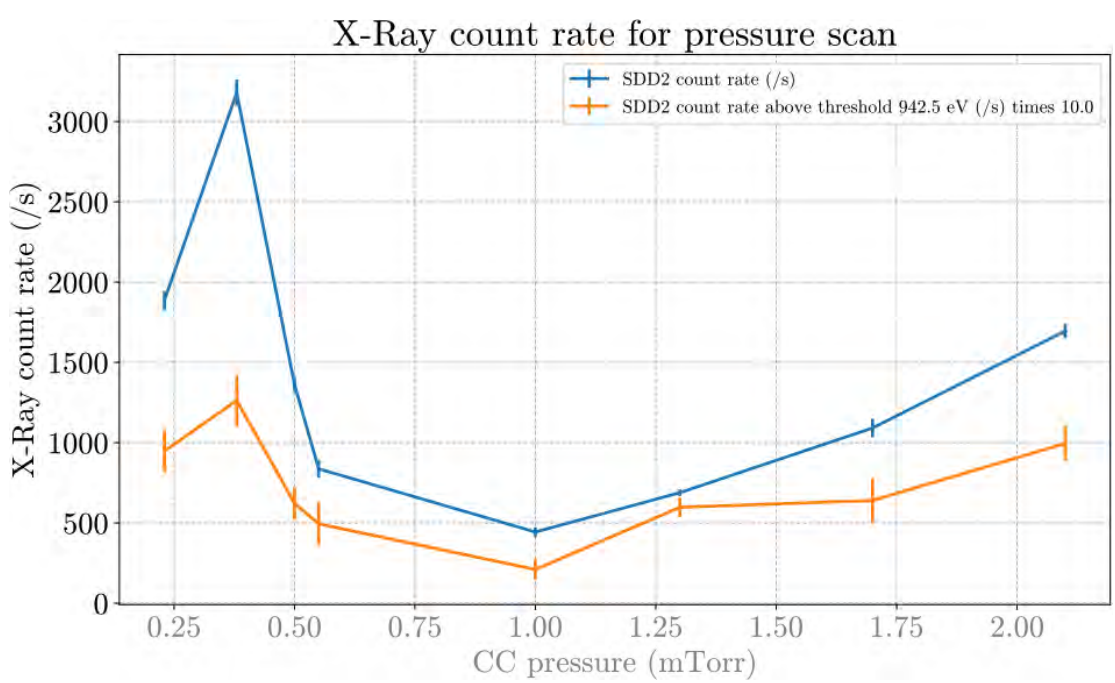

Figure 12. X-ray count rate vs. center cell pressure.

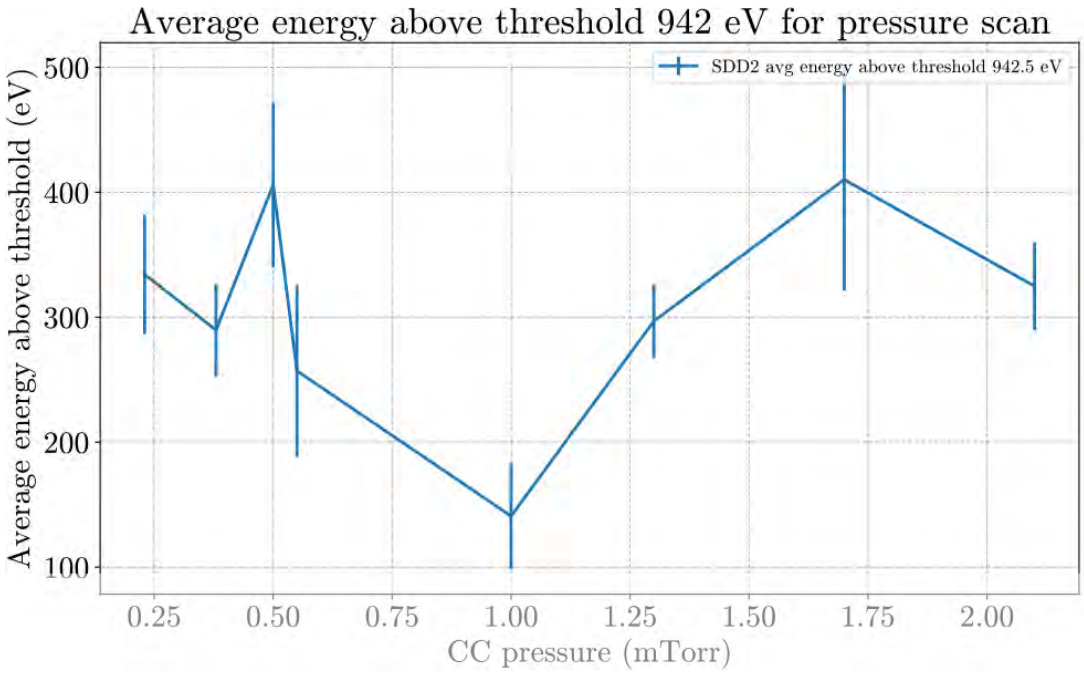

Figure 13. Average X-ray energy above 942 eV vs. center cell pressure.

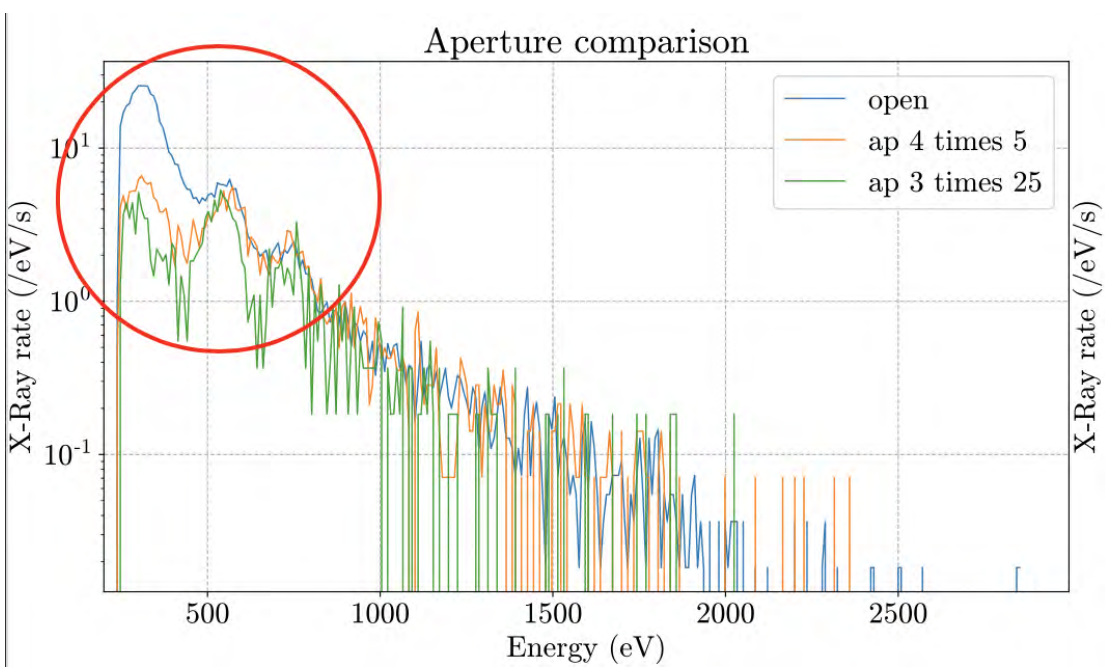

Figure 14. X-ray spectra recorded with the open aperture setting, the fourth aperture setting, and the third aperture setting, all at peaking time 200 ns.

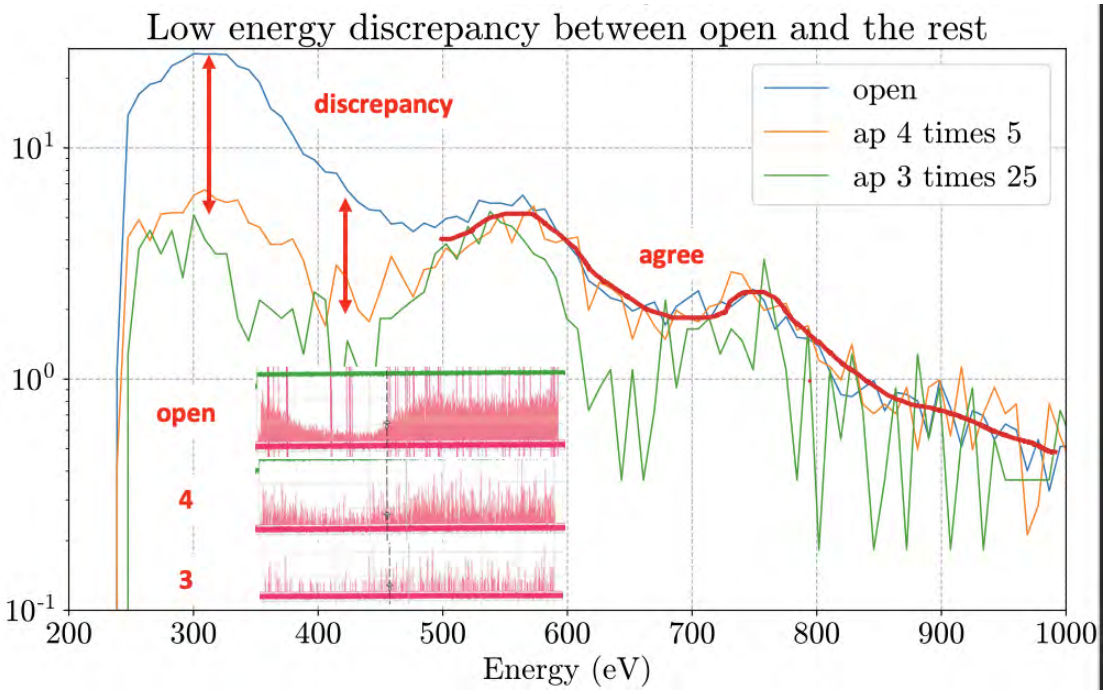

Figure 15. A close up of the discrepancy between the open aperture setting and the other settings.

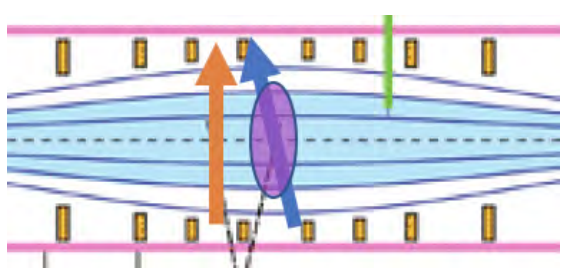

Figure 16. An oblate FRC, with the blue arrow being the line of sight of the midplane SDD.

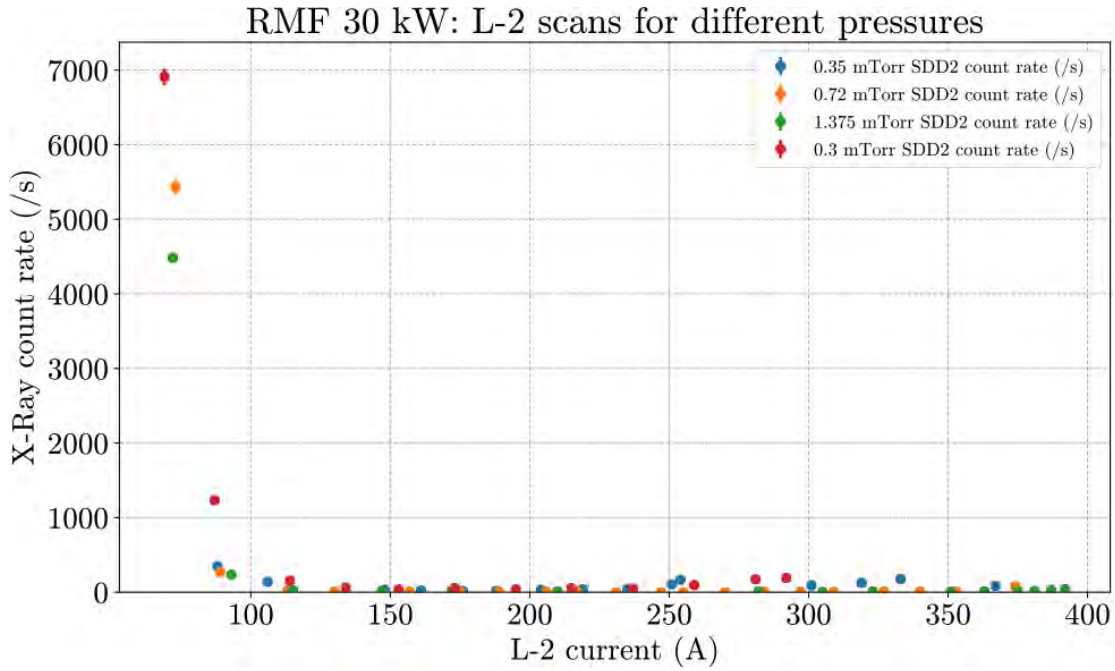

Figure 17. X-ray count rate vs. confining magnetic field for varying center cell pressure and 30kW RMF power.

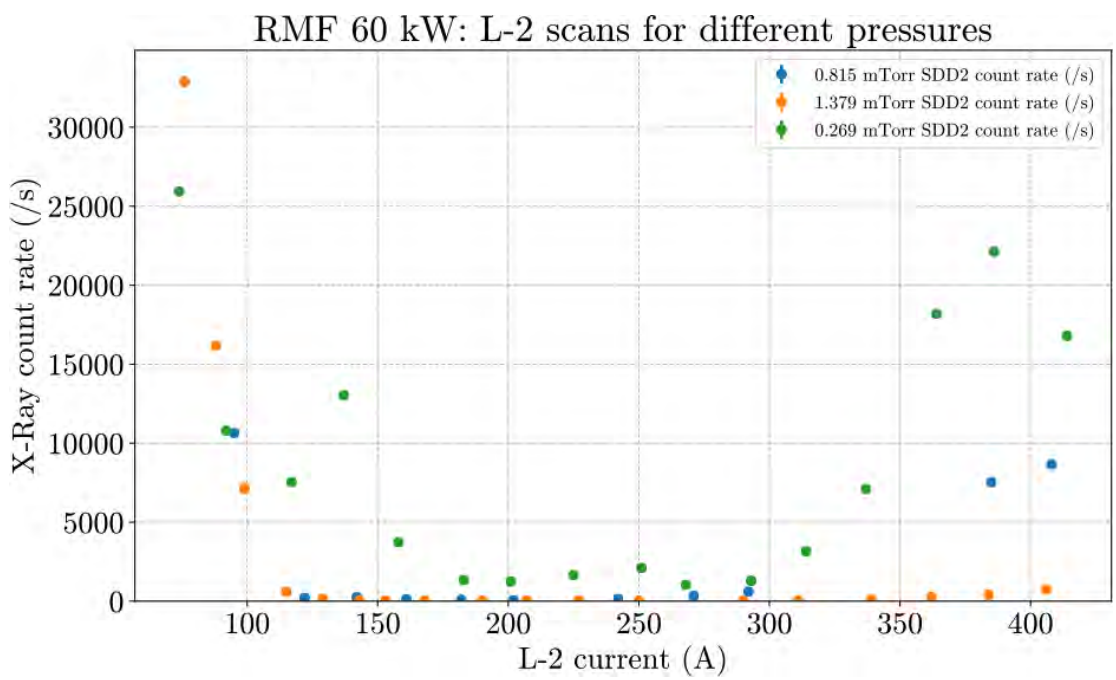

Figure 18. X-ray count rate vs. confining magnetic field for varying center cell pressure and 60kW RMF power.

scan with the 5cm displaced SDD, both an axial and radial profile of the FRC could be measured. The mechanism to move the magnetic minimum was simply changing the current in the belt coils. The amount by which to change the current to achieve a particular magnetic minimum, as well as the entire systematic new magnetic field configuration, was programmed in Python and computed.

Breaking the axis symmetry of the magnetic mirror of the PFRC-2 had not been done before. It was important to see if the the FRC could still form without this symmetry and whether or not a significant increase in nonadiabatic leakage of particles, as described by Reece Roth (1964) in the simplified case of a magnetic mirror without an FRC, would occur. Figure 21 shows the symmetric field lines at the center of the PFRC-2 without the belt coils, and Figure 22 shows the asymmetric field lines at the center of the PFRC-2 with the belt coils placed on the positive-z side. Field at the center is less steep. This addresses the conclusion by Balebanov and Semashko (1967) that increasingly steep rises in magnetic field of a magnetic mirror markedly lowers the charged particle lifetime. With a smaller field line gradient near the center of the z-axis from belt coils, it was predicted that confinement would increase because the charged particles would take longer to gyrate into the lower field paths until colliding into residual gas.

Figure 23 shows the belt coils installed and ready for experiment. They were made of AWG-6 wire with three groups of twelve windings, all connected in series to a 20V power supply. Each group was placed in between flux conservers at approximately 1", 2", and 3" along the positive z-axis. When not running current through the belt coils, their passive flux conserver properties are neglected due to the high conductivity of the flux conservers in place (Myers et al., 2012).

4.2 Belt Coil First Results

It was predicted that as the belt coil current was increased, the X-ray count rate in the midplane SDD would decrease and the X-ray count rate in the 5cm displaced SDD would increase. However, this was not observed in the first measurements. The 5cm displaced SDD measured the same near zero X-ray count rate for any value of belt coil current. Furthermore, the midplane SDD observed more high energy X-rays at a higher rate, as shown by the increase in both number of X-rays and the average energy above 1 keV in Figures 24 and 25. Figure 26 shows the high electron temperatures at high coil current calculated from the slope of the XEDF. A possible explanation for the increase in high energy X-rays observed is that the calculated location of the center of the FRC as a function of belt coil current was off. The presumed FRC could have shifted just enough to expose the midplane SDD to a hotter population of electrons that exists outside of the midplane. The existence of a hot population of electrons within the FRC was seen at 100x lower power by the helicon-antenna-formed seed plasma and 2x lower center cell pressure previously (Jandovitz et al., 2018). The possible explanation that the coils caused the plasma to interact more with the walls of the vacuum vessel and in turn produce more X-rays is disproven by the lack of Aluminum in the spectral signature observed in the XEDF, as Aluminum was pasted onto the wall to cover the line of sight of the midplane SDD.

4.3 Future Work

The next prototype of the PFRC must have higher confining magnetic field capabilities and lower RMF frequencies to heat and contain ions. As has been observed on the PFRC-2, simply increasing the field from the L-2 coils prevents the FRC from forming. Continuing the research on the belt coils, it is clear that another set of belt coils on the negative-z side to reestablish the symmetry of the magnetic field lines PFRC would create a higher magnetic field while still accommodating the FRC. As seen in Figure 27, the field lines do not bulge as much with the coils closer to the center. By reducing the bulge of magnetic field lines toward the center, the FRC has been observed to form better in the first results of asymmetric belt coils. Implementing symmetric belt coils is the next step in solving the problem of containing hotter ions with the hot electrons. With this setup, higher pressures and RMF powers must be explored to increase the temperature and density of the plasma in order to reach the critical values for fusion.

5 ACKNOWLEDGMENTS

I would like to thank Professor Sam Cohen for welcoming me into his project and for his guidance, insight, and support. I would also like to thank Bruce Berlinger for his technical expertise and support. I would also like to thank postdoctoral researcher Charles Swanson, graduate students Eugene Evans and Eric Palmerduca, and fellow interns Kai Torrens, Gabriel Gonzales, and Justin Cohen for their guidance and support.

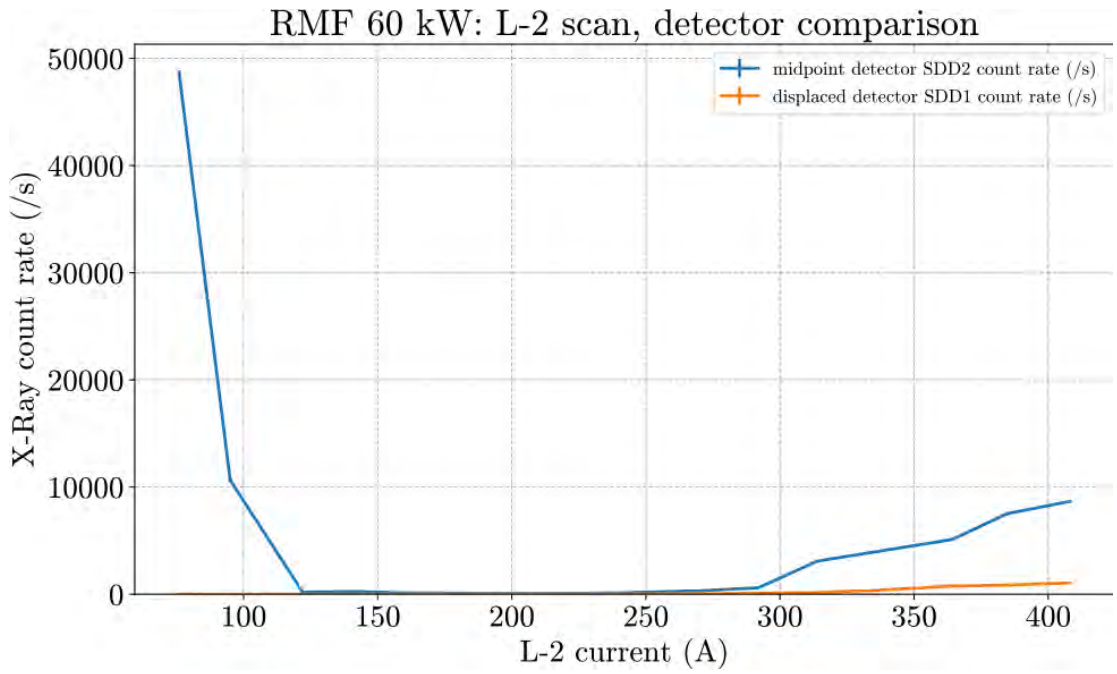

Figure 19. SDD in midplane and 5cm displaced (center-most orientation) comparison of X-ray count rate vs. confining magnetic field at 60kW RMF power.

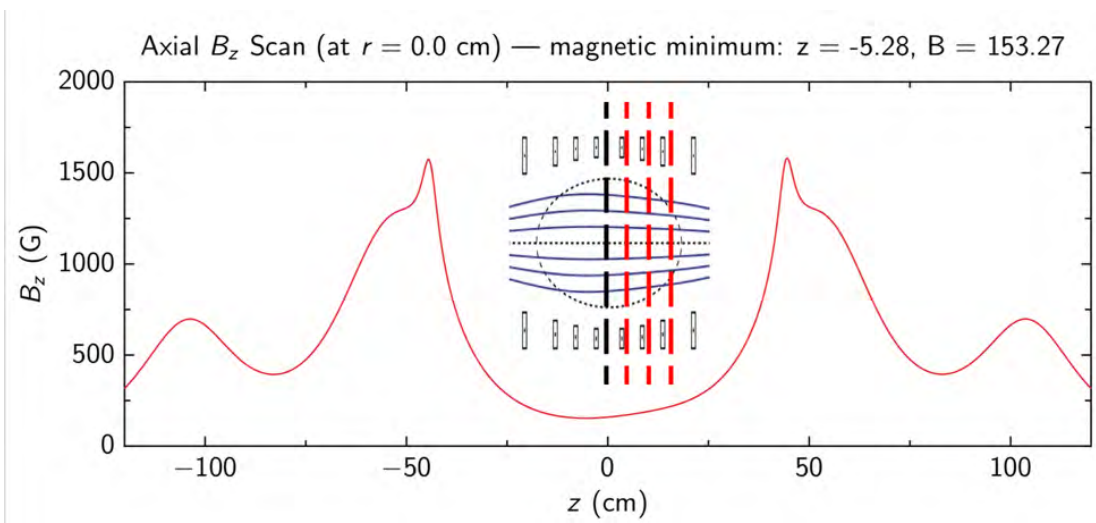

Figure 20. Axial magnetic field scan depicting the effect of the asymmetric belt coils setup.

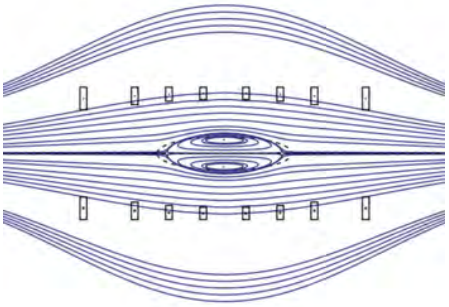

Figure 21. Magnetic field configuration around the midplane without belt coils added.

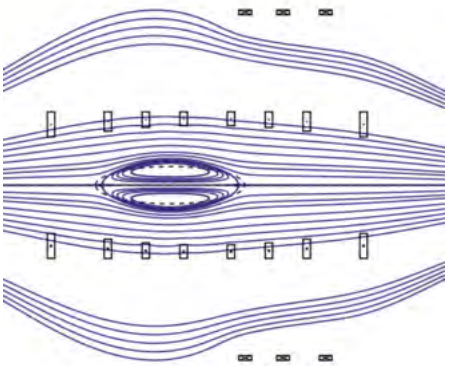

Figure 22. Magnetic field configuration around the midplane with the asymmetric belt coils added.

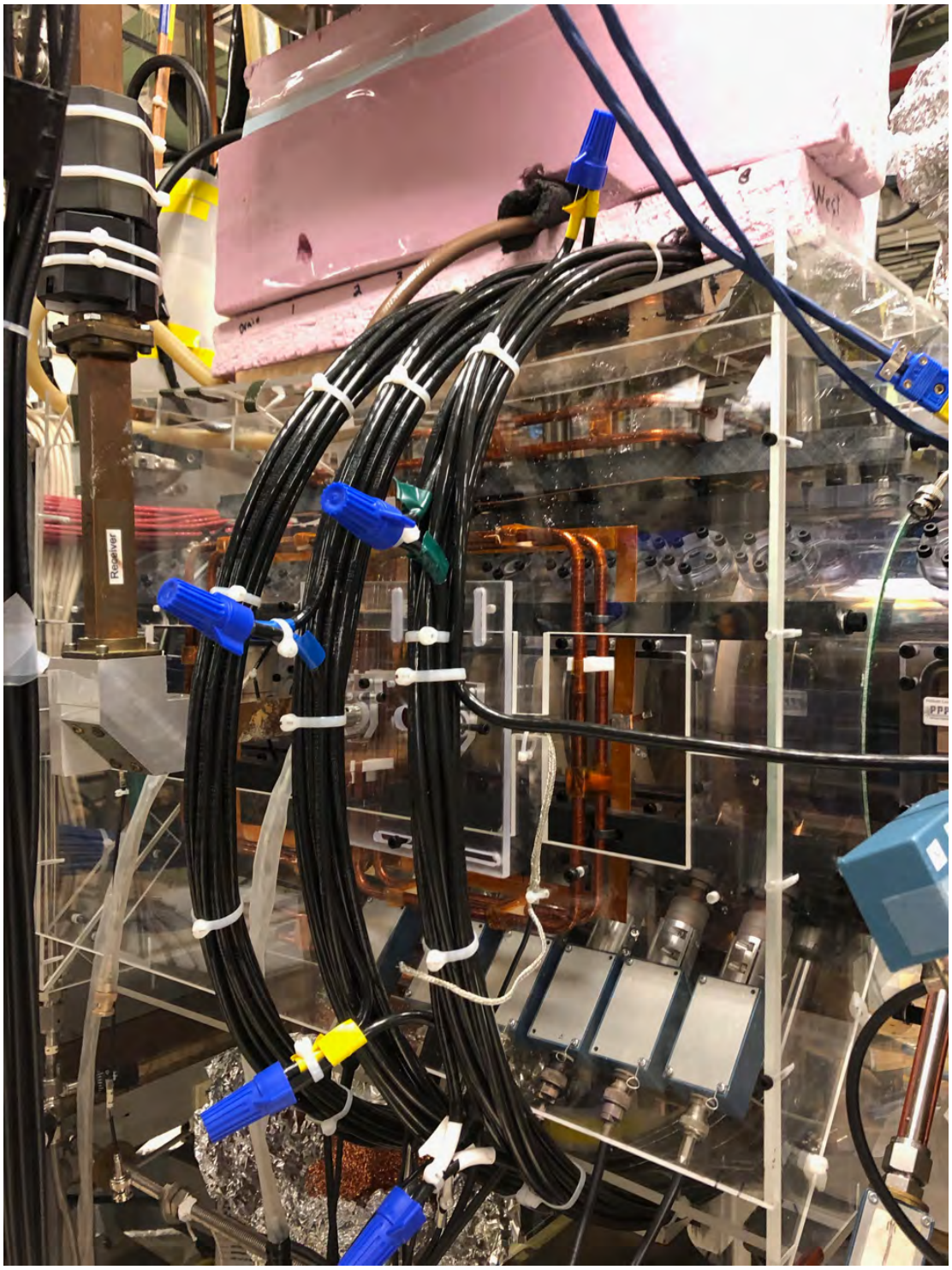

Figure 23. The asymmetric set up of belt coils installed onto the PFRC-2.

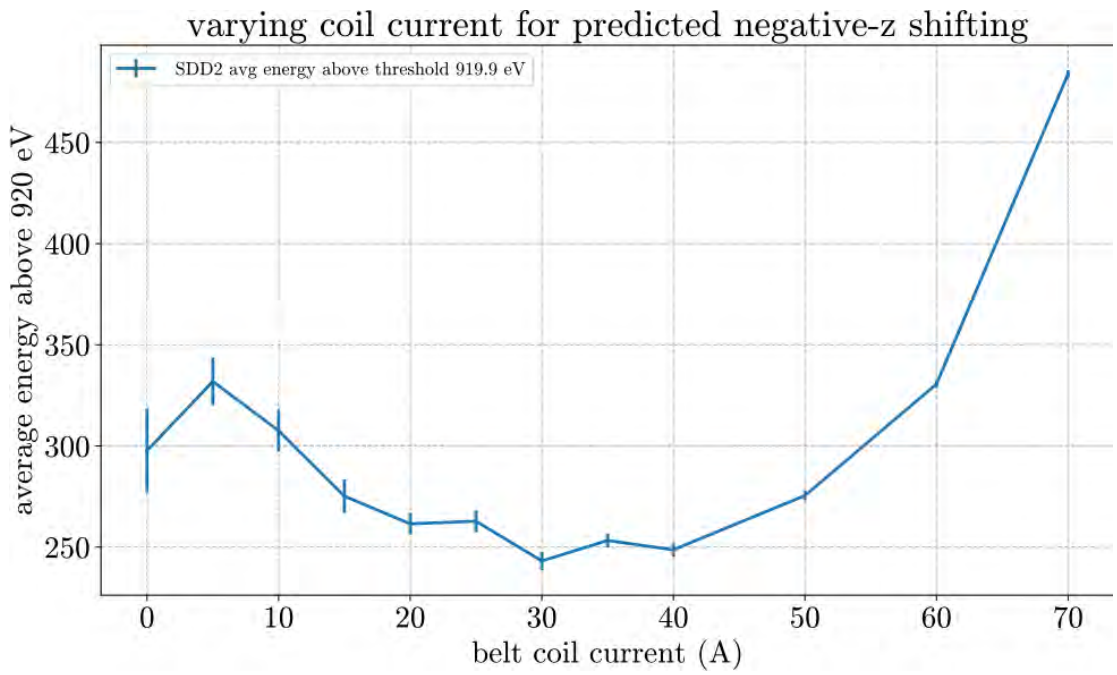

Figure 24. Average energy of incoming X-rays above the threshold 919.9 eV vs. belt coil current.

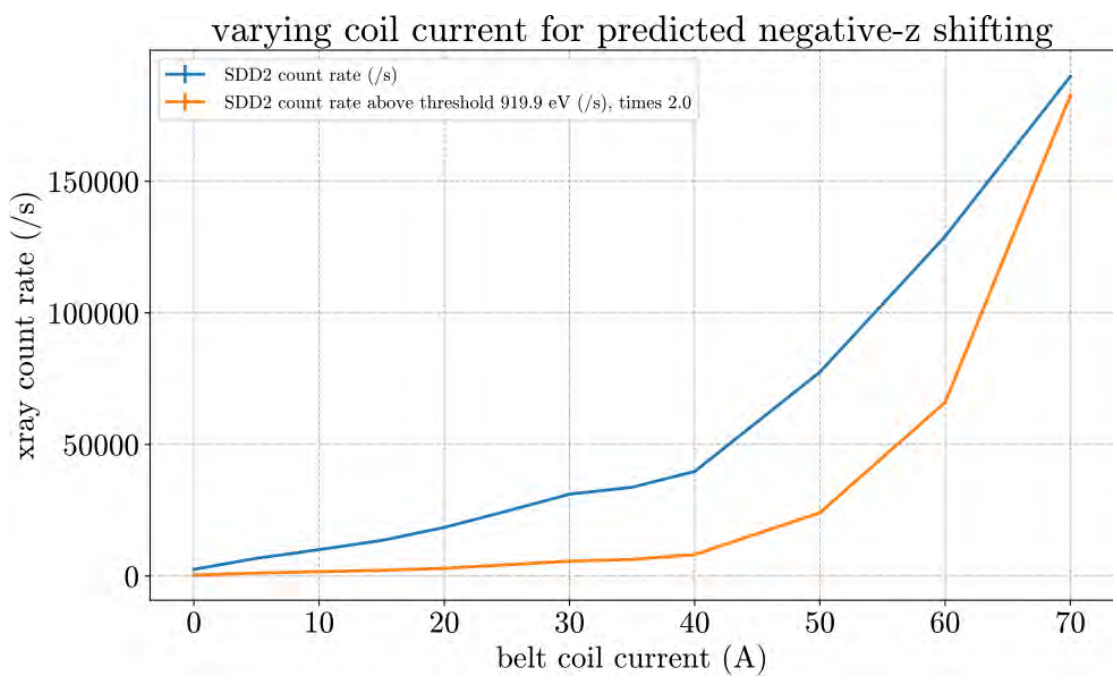

Figure 25. X-ray count rate vs. belt coil current, with rescaled (up factor of 2) high energy (¿919.9 eV) X-ray count rate.

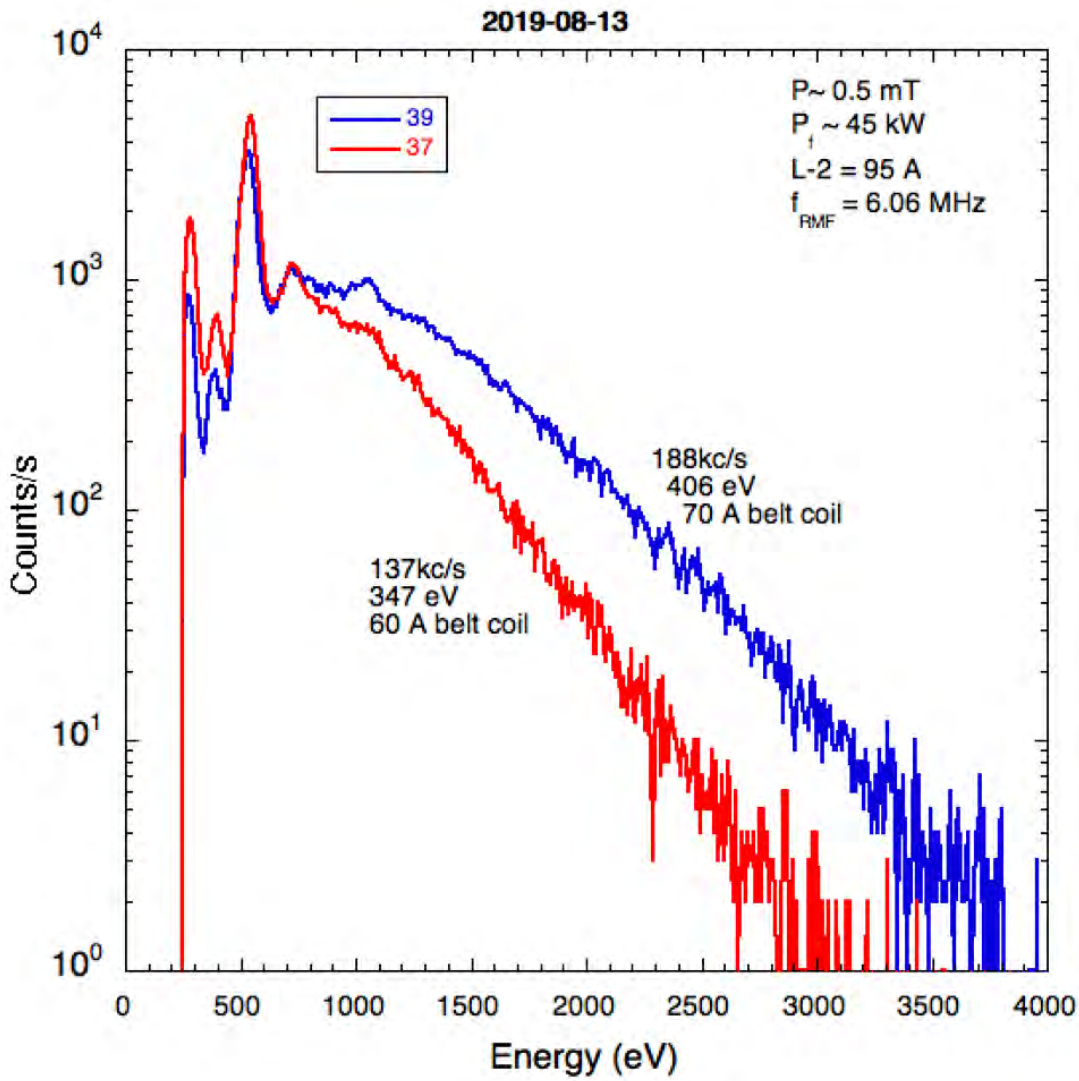

Figure 26. X-ray spectrum for two high values of belt coil current and clear difference in electron temperature.

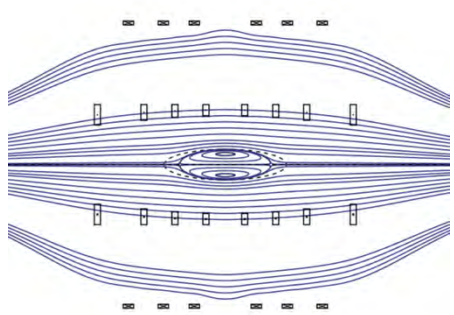

Figure 27. Magnetic field configuration around the midplane with the symmetric belt coils added.

REFERENCES

Balebanov, V. and Semashko, N. (1967). Lifetime of individual charged particles in a magnetic mirror trap. *Nuclear Fusion*, 7(4).

Cohen, S., Berlinger, B., Brunkhorst, C., Brooks, A., Ferraro, N., Lundberg, D., Roach, A., and Glasser, A. (2007). Formation of collisionless high-β plasma by odd-parity rotating magnetic fields. *Physical Review Letters*, 8(14).

Jandovitz, P., Swanson, C., Matteucci, J., Oliver, R., Pearcy, J., and Cohen, S. (2018). Demonstration of fast-electron populations in a low-pressure, low-power, magnetized rf plasma source. *Physics of Plasma*, 25(3).

Myers, C., Edwards, M., Berlinger, B., Brooks, A., and Cohen, S. (2012). Passive superconducting flux conservers for rotating-magnetic-field-driven field-reversed configurations. *Fusion Science and Technology*, 61.

Reece Roth, J. (1964). Nonadiabatic motion of a charged particle in an axisymmetric magnetic barrier. *The Physics of Fluids*, 7(4).

Swanson, C., Jandovitz, P., and Cohen, S. (2018). Using poisson-regularized inversion of bremsstrahlung emission to extract full electron energy distribution functions from x-ray pulse-height detector data. *AIP Advances*, 8(2).